Title	Hydrothermal Synthesis, Structure Investigation, and Oxide Ion Conductivity of Mixed Si/Ge-Based Apatite-Type Phases
Author(s)	Li, Henan; Baikie, Tom; Pramana, Stevin S.; Shin, J. Felix; Keenan, Philip J.; Slater, Peter R.; Brink, Frank; Hester, James; An, Tao; White, Timothy John
Citation	Li, H., Baikie, T., Pramana, S. S., Shin, J. F., Keenan, P. J., Slater, P. R., et al. (2014). Hydrothermal Synthesis, Structure Investigation, and Oxide Ion Conductivity of Mixed Si/Ge-Based Apatite-Type Phases. Inorganic Chemistry, 53(10), 4803-4812.
Date	2014
URL	http://hdl.handle.net/10220/39815
Rights	© 2014 American Chemical Society. This is the author created version of a work that has been peer reviewed and accepted for publication by Inorganic Chemistry, American Chemical Society. It incorporates referee's comments but changes resulting from the publishing process, such as copyediting, structural formatting, may not be reflected in this document. The published version is available at: [http://dx.doi.org/10.1021/ic402370e].

Hydrothermal synthesis, structure investigation, and oxide ion conductivity of mixed Si/Ge-based apatite-type phases

Henan Li,[a] Tom Baikie,[b] Stevin S. Pramana,[a] J. Felix Shin,[c] Philip J. Keenan,[c] Peter R. Slater,[c] Frank Brink,[d] James Hester,[e] Tao An[a] and Tim J. White*[a]

[a] *Nanyang Technological University, School of Materials Science and Engineering, 50 Nanyang Avenue, 639798, Singapore. Fax: +65 6790 9081; Tel: +65 6790 4586; E-mail: tjwhite@ntu.edu.sg*

[b] *Energy Research Institute @ NTU (ERI@N), Research Technoplaza, Nanyang Technological University, Nanyang Drive, 637553, Singapore.*

[c] *School of Chemistry, University of Birmingham, Edgbaston, Birmingham, B15 2TT, UK. Tel: +44(0)121 414 8906*

[d] *Centre for Advanced Microscopy, R N Robertson Building (Bldg 46), Sullivan's Creek Road, The Australian National University, Canberra ACT 0200. Tel: +61 (0)2 6125 6883*

[e] *Australian Nuclear Science and Technology Organisation (ANSTO), New Illawarra Road, Lucas Heights NSW 2234 Australia. Tel: +61 (0)2 9717 9907*

Keywords: Apatite; Solid oxide fuel cell; Electrolyte; Hydrothermal synthesis; Crystal chemistry; Microscopic structure; Ionic conductivity

Abstract

Apatite-type oxides ($[A^{I}_4][A^{II}_6][(BO_4)_6]O_2$), particularly those of the rare earth silicate and germanate systems, are among the more promising materials being considered as alternative solid oxide fuel cell (SOFC) electrolytes. Nonstoichiometric lanthanum silicate and germanate apatites display pure ionic conductivities exceeding those of yttria-stabilized zirconia (YSZ) at moderate temperatures (500 – 700 ºC). In this study, mixed Si/Ge-based apatites were prepared by hydrothermal synthesis under mild conditions, rather than the conventional solid-state method at high temperatures. Single-phase and highly-crystalline nanosized apatite powders were obtained with the morphology changing across the series from spheres for the Si-based end-member to hexagonal rods for the Ge-based end-member. Powder X-ray and neutron analysis found all these apatites to be hexagonal ($P6_3/m$). Quantitative X-ray microanalysis established the partial (< 15 at%) substitution of La^{3+} by Na^{+} (introduced from the NaOH hydrothermal reagent) that showed a slight preference to enter the A^{I} 4*f* framework position over the A^{II} 6*h* tunnel site. Moreover, retention of hydroxide (OH^{-}) was confirmed by infrared spectroscopy and thermogravimetric analysis, and these apatites are best described as oxy-hydroxyapatites. To prepare dense pellets for conductivity measurements, both conventional heat treatment and spark plasma sintering methods were compared, with the peculiar features of hydrothermally synthesized apatites and influence of sodium on ionic conductivity considered.

1. Introduction

Rare-earth silicates and germanates adopting the apatite-type structure have attracted widespread interest as electrolytes for solid oxide fuel cells (SOFCs), as they are superior ionic conductors compared to yttria stabilized zirconia (YSZ) at moderate temperatures (< 700 ºC).[1-6] The general formula for electrolyte oxyapatite is $[A^{I}_4][A^{II}_6][(BO_4)_6]O_2$, where *A* are rare-earths or alkaline-earths and *B* is Si or Ge. A wide range of chemical substitutions and non-stoichiometry (cation vacancies and/or oxygen excess) can be adjusted to modify ion migration and electrical properties.[7-16] It is well established that ionic conductivity for A^{I} cation deficient phases is significantly higher than in stoichiometric materials,[17-20] and that larger A^{II}/A^{I} species promote oxygen migration through lower activation energy.[21] Consequently, the larger lanthanum (La^{3+}) apatite analogues usually show superior electrolyte performance, compared to smaller rare earth (Yb^{3+}) compounds.[22, 23]

Apatites are generally $P6_3/m$ hexagonal with an $A^{I}_4(BO_4)_6$ framework surrounding the $A^{II}_6O_2$ tunnel contents where the oxygen atoms notionally occupy the centre of [0 0 1] one-dimensional channels at 0, 0, *z* (4*e* according to Wyckoff notation).[21, 24] The rare-earth cations (La^{3+}) are located at the 6+3-coordinated A^{I} position (4*f*, (1/3 2/3 *z*)) and the A^{II} site (6*h* (*x y* 1/4)) bonded to 7 oxygen, whereas *B* cations (Si^{4+}/Ge^{4+}) occupy the 4-coordinated 6*h* (*x y* 1/4) sites. It is instructive to describe the framework as a motif of $A^{I}O_6$ metaprisms that are corner-connected to BO_4 tetrahedra to create adaptive tunnels that expand or contract by tuning the metaprism twist angle (ϕ).[21, 24] Both the framework and tunnel show varying degrees of nonstoichiometry, with cation vacancies concentrated at the framework A^{I} position. The *B*-site is apparently fully occupied, but the coordination to oxygen is variable with MAS-NMR and neutron diffraction revealing BO_5 and BO_6 polyhedra in addition to the BO_4 tetrahedra. In the Ge containing apatites, these GeO_5 polyhedra serve to accommodate

oxygen interstitials necessary for ion migration.[25-28] In the Si containing apatites, a number of possible sites have been proposed for the location of the oxygen interstitials ranging from the centre of the channel to close to the SiO_4 tetrahedra In addition, B_2O_7 dimers have been suggested as a way to stabilize A^I vacancies.[29]

Apatite electrolytes are mostly obtained at high temperatures (> 800 ºC) through calcination of homogeneous precursor powders prepared by grinding oxides or sol-gel methods.[1, 30] The synthesis of Ge-containing apatites is somewhat problematic, as compared to silicates, due to Ge volatilization leading to mixed phase products.[9, 31-34] Recently, a mild hydrothermal synthesis of silicate oxy-hydroxyapatites was found to deliver a pure and highly crystalline product at low temperature (230 ºC).[35, 36] To date however, there is a lack of systematic studies to establish the optimal hydrothermal conditions for silicate apatite preparation, and analogous germanates have not been produced in this way. Here, we targeted mixed Si/Ge-based lanthanide apatites of composition $La_{9.33}Si_{6-x}Ge_xO_{26}$, for hydrothermal synthesis, with subsequent studies of crystal chemistry, defect concentration and powder morphology used to explore the relationship between structure and ionic conductivity. It was found that germanate apatites are superior electrolyte materials, but for hydrothermally prepared materials care is needed to control sodium contamination, which lowers the total oxide ion content, and hence also the conductivity.

2. Experimental methods

2.1 Synthesis

Apatites of nominal composition $La_{9.33}\square_{0.67}Si_{6-x}Ge_xO_{26}$ ($\square$ represents A^I vacancies, $0 \leq x \leq 6$) were hydrothermally synthesized from gels with the chemical composition (molar ratio) of 2.5-4.1La_2O_3:5.3(SiO_2+GeO_2):19.3Na_2O:1722H_2O. The amount of lanthanum was adjusted empirically to obtain single-phase apatites. In a typical synthesis with Si/Ge=1, 2.13 g of $La(NO_3)_3 \cdot 6H_2O$ (Strem, 99.9%) was dissolved in 13 ml of de-ionized (DI) water (Solution I). Subsequently, 0.16 g of silicic acid (Merck, 99%) and 0.28 g of GeO_2 (Alfa, 99.999%) were dissolved in the base solution containing 1.54 g of NaOH (Schedelco, 99.9%) in 18 ml of DI water (Solution II). These stock solutions were combined by introducing Solution I to Solution II dropwise, with stirring continued for two hours at ~70 ºC to ensure a homogeneous gel was formed. This mixture was sealed in a 45 ml Teflon-lined stainless steel autoclave and reconnaissance crystallization performed at 180–240 ºC from 3 h to 60 days. Based on yield and crystallinity, a static condition of 240 ºC / 16 hours was selected for bulk synthesis of powders used for X-ray and neutron powder diffraction and ionic conductivity tests. After cooling to room temperature the product was centrifuged, washed with DI water and dried at 60 ºC overnight. The overall ideal reaction can be expressed as:

$$9.33\ La(NO_3)_3 \cdot 6H_2O + (6 - x)\ SiO_2 + x\ GeO_2 + 28\ NaOH \rightarrow$$

$$La_{9.33}Si_{6-x}Ge_xO_{26} + 28\ NaNO_3 + 14\ H_2O + 55.98\ H_2O \text{ where } 0 \leqslant x \leqslant 6. \quad (1)$$

The situation is not as straightforward as Equation (1) suggests, since apatites contain several cation acceptor sites leading to a wide range of substitutional possibilities[24], and as

considered shortly, monovalent Na^+ ions can potentially displace La^{3+}. Both H^+ and OH^- ions could also be incorporated.

2.2 Powder diffraction

Laboratory powder X-ray diffraction (XRD) patterns were acquired at room temperature using a Bruker D8 Advance diffractometer fitted with a LynxEye silicon strip detector. Data were accumulated with CuK_α (λ_{av} = 1.541874 Å) radiation (40 kV, 40 mA), coupled θ - 2θ geometry over the angular range 10° < 2θ < 130°, and a step size of 0.02° with a counting time of 1 s per step. The specimens were prepared by pressing powders into PMMA rings (Ø = 25 mm). While XRD delivers accurate lattice parameters, the technique is insensitive to oxygen in the lanthanum-rich matrix, and to arrive at more complete crystallographic descriptions, neutron powder diffraction was undertaken using the Echidna[37] (high resolution powder diffractometer) beamline at ANSTO (Australian Nuclear Science and Technology Organisation) drawing neutrons from the Open Pool Australian Lightwater (OPAL) reactor. A Ge (335) monochromator with 140° take-off angle yielded a wavelength of 1.622 Å. The samples were contained in vanadium cans (10 mm in diameter) and data was collected at ambient temperature over the range of 4-164° 2θ with a step size of 0.05° for 3 h. In order to gain additional information on the effect of water incorporation and possible loss at elevated temperature, the silicate and germanate end-members were subjected to *in-situ* high temperature neutron diffraction studies from 25 to 1100 ºC.

2.3 Electron microscopy and electron probe microanalysis

For scanning electron microscopy (SEM), secondary electron and backscattered electron images were collected using a JEOL JSM 7600F microscope. The samples were embedded

in thermal epoxy resin disks (diameter 25 mm and thickness 5 mm), mirror-polished and carbon coated for quantitative analyses, and data was collected at 15 kV and 1 nA using a JEOL JSM 6400 SEM equipped with an Oxford Instruments light element energy dispersive spectrometer (EDS) and Link ISIS SEMquant software. To confirm the bulk composition, electron probe microanalysis (EPMA) was performed for three selected samples on a JEOL JXA-8530F equipped with five wavelength dispersive spectrometers (WDS). The accelerating voltage and current used were 10 kV and 40 nA, respectively. Standards employed were monazite (La) and albite (Na, Si and Al) minerals obtained from Astimex, while synthetic GeO_2 (Ge) was from Alfa Aesar. The peak counting time for La, Na, Si, Al and Ge was 30, 60, 30, 60 and 30s, respectively and the background counting time was half of the characteristic peak. For transmission electron microscopy (TEM) the apatites were finely ground under ethanol and ultrasonically dispersed for ~10 min, then several drops of the suspension were deposited on a holey carbon film supported by a copper grid that was air-dried before introduction to the microscope. High-resolution (HR) images and selected area electron diffraction (SAED) patterns were collected using a JEOL JEM-2010 operated at 200 keV.

2.4 Fourier transform infrared spectroscopy and thermogravimetric analysis

Fourier transform infrared (FTIR) spectra of powdered samples suspended in potassium bromide (KBr) pellets were acquired at room temperature from 400 and 4000 cm^{-1} using a Perkin Elmer (Spectrum 2000) spectrophotometer with a spectral resolution of 4 cm^{-1}. The water contents were assessed through thermogravimetric analysis (TGA) using a Mettler Toledo TGA/SDTA 851 instrument. The experiments were carried out in air with a heating rate of 10 ºC/min up to 1000 ºC.

2.5 Impedance spectroscopy

For conductivity measurements, conventional compact pellets (10 mm diameter) were prepared as follows: the apatite powders were mixed with binder (isopropyl alcohol with 3% polyvinyl butyral), pelletised (300 bar) uniaxially, and sintered at 1500 ºC for six hours. Both sides of the pellets were coated with Au paste and then heated to 750 ºC to ensure bonding to the pellet. For comparison, spark plasma sintering (SPS),[38-40] a hot-pressing technique with a high heating rate, was applied to fabricate dense (> 95% theoretical density (TD)) polycrystalline pellets using a Dr Sinter SPS-825 (SPS Syntex Inc., Japan) apparatus. Apatite powders were loaded in a Ø 20 mm graphite die set and uniaxially pressed at a constant pressure of 50 MPa during the entire process. The temperature was first ramped to 600 ºC at a rate of 150 ºC/min, and then to 850 ºC at a rate of 100 ºC/min. After this rapid heating, the temperature was slowly raised to 950 ºC in 3 min, with increments of 50 ºC, 30 ºC and 20 ºC in each respective minute. The sample was pressed for 5 min at this temperature for the sintering to complete, after which both pressure and heating power were released for the samples to cool naturally. Finally, the materials were burnt in air at 850 ºC for 2 h to remove residual carbon. For both type of pellets, the ionic conductivity was evaluated by alternating current (AC) impedance spectroscopy (Hewlett Packard 4192A impedance analyzer), with measurements taken in air, with an applied voltage of 0.1 V over a frequency range of 100 Hz – 10 MHz from 300 to 800 ºC. The impedance spectra showed a single broad semicircle consistent with a combination of bulk and grain boundary components, and so it was not possible to accurately extract individual bulk resistivities. Consequently the data reported represent total conductivities.

3. Results and discussion

3.1 Synthesis and phase assemblage

Laboratory powder X-ray diffraction patterns confirmed the synthesis of a single phase apatite for the Ge end-member when the reaction was conducted above 200 ºC; for synthesis at 240 ºC the single-phase product formed within 3 hours. The Si end-member was obtained similarly. Based on a fixed ratio of Si/Ge sources and base concentration, the introduced La content was always < 85% of the stoichiometric quantity, as preliminary experiments found stoichiometric combinations produce significant amounts of secondary phases (mainly the unreacted $La(OH)_3$), and although longer synthesis times reduced these, they were not eliminated completely even after 60 days reaction (Fig. S1, Supporting Information). Because SiO_2 and GeO_2 dissolve in hot (~80 ºC), concentrated NaOH while $La(OH)_3$ precipitates, extra-stoichiometric Si and Ge oxides are required to promote the fast crystallization of apatite. After many trials, it was concluded that with the La source fixed at 60% of the stoichiometric value, the optimized condition of 240 ºC and 16 hours produced well crystallized single-phase apatite across the whole mixed Si/Ge series. These parameters are more robust than reported previously[35, 36] (230 ºC / 6 days), and there remains a degree of flexibility to choose various combinations of temperature, time, stoichiometry and reagent-to-water ratio to manipulate crystal size and morphology.

3.2 Microstructure and local structure

Backscattered electron images of the apatite powders found the Si end-member composed of spherical nanoparticles (30 – 100 nm), but as the Ge content increased, the average particle size increases (~40 to 200 nm), and the spherical crystals elongate, until for the germanate end-member, the crystals become hexagonal rods (100 – 600 nm) (Fig. 1). The

microstructures for apatites synthesized under different conditions are collated in Fig. 2, and while growth is slow, the rod length increases by an order of magnitude (from 100 nm to several microns) after 60 days. Single-phase germanate apatite forms at 220 ºC and 240 ºC, but at < 200 ºC, the large hexagonal apatite rods co-exist with acicular $La(OH)_3$.

To confirm the particles are well crystallized, SAED and phase contrast imaging was carried out for the two end-members and one intermediate composition (x = 3) (Fig. 3). The microstructures shown in the low-magnification images are consistent with the BEI images. HRTEM contrast was not uniform as rapid damage under the highly energetic electron probe may arise from volatilization of hydrogen-bearing species.

3.3 Hydroxyl incorporation — FTIR spectroscopy and TGA

The FTIR transmission spectra across the Si/Ge series (Fig. 4) contains a broad band from 2600 to 3700 cm^{-1} arising from hydroxyl groups and water, but distinct from calcium phosphate hydroxyapatite, the O-H bond stretching mode does not appear as a narrow peak[41] at ~3570 cm^{-1} and the OH librational mode (~630 cm^{-1}) was not detected. These differences are suggestive of a low OH^- ion content that are consistent with the previous research[35, 36] indicating the coexistence of OH^- and O^{2-} ions and the formation of oxy-hydroxyapatites. The bands at 962 and 910 cm^{-1} belong to asymmetric stretching modes of the SiO_4 group, while those at 542 and 490 cm^{-1} result from asymmetric bending modes of the SiO_4 group and La-O vibration modes.[42, 43] Analogously, the bands at 786, 764, 451, 416 cm^{-1} are assigned to the stretching and bending modes of the GeO_4 group but moved to shorter wavenumbers compared to SiO_4.[31] Further evidence of the presence of hydrous species was obtained by TGA (Fig. 5) with significant weight losses (~2%) observed; the initial ~1.3% weight loss up to 300 ºC should be due to evaporation of absorbed and crystalline H_2O, and

the subsequent minor loss till 1200 ºC could be caused by removal of OH groups, accompanied by conversion to oxyapatite.

3.4 Crystal chemistry

Quantitative microanalyses (Table 1) were performed by SEM-EDS and EPMA; aside from establishing the La/Ge/Si content, these analyses were used to investigate the incorporation of sodium. There is an apparent deviation from the nominal compositions, which correlates well with the refined compositions from Rietveld analysis. The La content is lower than expected, which is attributed to the incorporation of Na, and through the whole series, the Si/Ge ratio is larger than nominal values. As both silicon and germanium were always in excess with respect to the lanthanum source and the dissolution kinetics of SiO_2[44] and GeO_2[45] are distinct, some departure from nominal product compositions is expected. As the Ge content increases, the Si/Ge ratio approaches its putative value. It is noted that minor Si (< 0.2 wt.%) was detected in the germanate end-member, and is probably introduced by corrosion of glass containers used for the strong alkaline solution. Because of the close characteristic X-ray line energies for Na ($K\alpha_{1,2}$ 1.041 keV), La ($M\alpha_1$ 0.833 keV) and Ge ($L\alpha_{1,2}$ 1.188 keV),[46] the Na contents detected by EDS are potentially inaccurate. However, these characteristic X-rays are readily separated by wavelength dispersive X-ray analysis (Na = 1.192 nm; La = 1.490 nm; Ge = 1.045 nm), and for confirmation, EPMA on three selected samples (two end-members and one mixed Si/Ge of nominal x = 3) were performed and the analyses found in reasonable agreement with EDS (Table 1).

Several charge balance mechanisms can be formulated to accommodate sodium. As the ionic radii of La^{3+} (CN 6, 1.03Å) and Na^+ (CN 6, 1.02Å) are similar,[47] monovalent Na^+ ions may

substitute for trivalent La^{3+} by creating oxygen vacancies (Equation (2)), or occupy La^{3+} cation vacancies together with the incorporation of oxygen interstitials (Equation (3)).

$$La^{3+} + O^{2-} \rightarrow Na^{+} + \square_{O^{2-}} \quad (2)$$

$$2\square_{La^{3+}} + \square_{O_i^{2-}} \rightarrow 2Na^{+} + O_i^{2-} \quad (3)$$

A general scheme that includes (2) and (3) can be written as:

$$La^{3+} + 2\square_{La^{3+}} \rightarrow 3Na^{+} \quad (4)$$

Driven by the charge balancing and characteristics of the synthesis method, it is possible that hydrogen is involved in the form of hydroxide and the valance imbalance caused by sodium substitutions could be solved by replacing oxygen with hydroxide ions (Equation (5)).

$$La^{3+} + 2O^{2-} \rightarrow Na^{+} + 2OH^{-} \quad (5)$$

3.5 Rietveld refinement and crystal structures

The powder X-ray data were refined with TOPAS[48] and the starting composition of $La_{9.33}Ge_6O_{26}$ in space group $P6_3/m$ (No. 176). A fundamental parameter peak function was adopted and the background (four-coefficient Chebychev polynomial and 1/x profile), zero error, scale factors, and lattice dimensions were refined sequentially followed by [La/Na] and [Si/Ge] fractional occupancies, atom positions and isotropic atomic displacement parameters (ADPs). The refinement of neutron diffraction data was conducted with JANA2006[49] using the same starting model, but the profile fitting was performed with a pseudo-Voigt peak shape function and a five-coefficient Chebychev polynomial background, while simultaneously refining the lattice and zero shift parameters. Finally, the occupancies, atom fractional coordinates and anisotropic ADPs were released simultaneously to complete the crystal structure modeling. In some cases, the O(1), O(3) tetrahedral oxygen gave non-physical ADPs and in these instances, the isotropic displacement parameter was used.

Similar observations were made by An *et al*.[50] and Orera *et al*.[51] in their analyses of electrolyte apatites, that are believed to be an artifact of tetrahedral disorder.

All the profiles were satisfactorily modeled in $P6_3/m$ with low R_{wp} values (< 6%) for both X-ray and neutron data (Fig. 6). The refined lattice parameters ($a = b$, c) and unit cell volumes dilate linearly with increasing Ge content (x) as Ge^{4+} (CN 4, 0.39Å) has a larger ionic radius than Si^{4+} (CN 4, 0.26Å)[47] (Table 2, Fig. 7).

As the Na^+ ions could reside on both 6*h* and 4*f* sites, the occupancies of La^{3+} and Na^+ were allowed to vary, with the constraint of full occupation applied to the 6*h* [La/Na], but not to the 4*f* [La/Na] site, as vacancies usually appear at the latter position. To maintain neutrality, the substitution of monovalent Na^+ cations on trivalent La^{3+} sites may be balanced by the creation of anionic vacancies. As the FTIR data indicated the existence of –OH groups, the incorporation of OH^- ions at the expense of O^{2-} ions should also be taken into account. The overall effect makes the expression of the chemical compositions in hydrothermal products rather more complex, as compared to solid-state synthesized apatites, and these phases are best described as oxy-hydroxyapatites, however, the details cannot be established by X-ray diffraction. More directly, the 6*h* [Si/Ge] sites can be regarded as fully tenanted and the average scattering power of the tetrahedrally coordinated cation is readily determined.

As neutron diffraction is better able to detect light elements (O and H), this technique was ultimately used for the final structural analysis. To model the tunnel oxygen, the 2*a* site was initially selected, but Fourier mapping showed a pair of symmetrical excess scattering centers along *z* (Fig. 8 (A) & (C)), that could be accounted for using a 4*e* position with a refined occupancy of ≤ 50%. For all other oxygen positions full occupancies were appropriate. The

remaining negative peaks around the tunnel center (0 0 0) in the Fourier map could be accounted for by placing H^+ ions at these positions (Fig. 8 (B) & (D)). This finding is consistent with crystal chemistry and the demand for charge balance.

The refined occupancies yielded 2 – 9% vacancies on A^{I} (4*f*) site. Moreover, the partitioning of Na^+ across A^{I} (4*f*) and A^{II} (6*h*) sites was almost equal, with a slight preference for the A^{I} framework site (Table 3). The chemical compositions derived from Rietveld analysis were generally consistent with EDS/EPMA chemical analyses. However, the complexity of La/Na/□ and O/OH/□ distributions and occupations mean the chemistries established by Rietveld refinement do not exactly charge balance. Taking the nominal x = 3 as an example, the refined composition is $La_{8.40}Na_{1.31}Si_{4.70}Ge_{1.30}O_{25.58}H_{0.44}$ (overall charge = -0.21) while charge balanced expression would be $La_{8.40}Na_{1.31}Si_{4.70}Ge_{1.30}O_{24}(OH)_{2.51-2y}O_y\square_{y-0.51}$. The whole analogue can be represented as $La_{8.50}Na_{1.29}Si_{6-x}Ge_xO_{24}(OH)_{2.79-2y}O_y\square_{y-0.79}$ by taking the average La and Na content of the 7 samples.

The atomic displacement parameters (Table 4) of the channel oxygens (4*e*) showed significant anisotropy with high U_{33} displacements suggestive of diffusion along the channel, or the presence of OH groups displaced off the ideal site to allow for efficient hydrogen bonding to neighbouring oxide ions.[52] Large oxygen ADPs are indicative of average scattering of the Si/GeO_4 tetrahedra, as a result of stoichiometric mixing of Si and Ge, together with cooperative relaxation of the BO_4 units that facilitates oxygen ion migration. In addition, the small positive scattering centers inside the tunnels located by Fourier mapping supports the presence of a low concentration of interstitial sites at the channel periphery. This is consistent with previous studies of $La_{9.33}Si_6O_{26}$ that linked these interstitial sites to silicate sublattice distortions. As expected, the smaller Si has a significantly lower bond

valence sum (BVS) compared to Ge, while the La^{I} atom in the metaprism is underbonded and Na is slightly overbonded. The average BVS for A^{I} and *B* sites are close to ideal with 2.35/2.43 and 4.24/4 for the composition of $La_{8.40}Na_{1.31}Si_{4.70}Ge_{1.30}O_{25.58}H_{0.44}$ (Table 5).

The *in-situ* high temperature neutron diffraction studies proved the loss of hydroxyl species at elevated temperatures because the profile background, with a significant incoherent scattering component from ^{1}H, decreases through the whole process (Fig. S2, Supporting Information). The major loss was found within 300 ºC, which is consistent with the result from TGA. The refined neutron diffraction data collected at 1100 ºC showed obvious proton loss and oxygen enrichment (Table S1, Supporting Information), and more free charge carriers could thus be obtained by the oxidization of the apatites.

3.6 Oxide ion conductivities

Pellets prepared by conventional sintering showed poorer conductivity (Table 6) , in line with prior studies of apatite systems, where the comparatively low temperature (particularly for the Si rich samples) and the short heat treatment (6 h) to limit Ge loss, was insufficient for full densification. The recorded conductivities are comparatively low for apatite silicate/germanate electrolytes. Starting from the silicate end-member, the conductivity does not change appreciably with Ge doping until $x = 3$, with an obvious increase for $x \geq 4$ that continues to the Ge end-member (Fig. 9 (A)). This observation can be partly attributed to trends in pellet density, as the silicate rich electrolytes have lower density (< 85% TD) while the germanate rich electrolytes show significantly improved density (up to 97% TD). A major factor, however, affecting the conductivities is likely to be the incorporation of Na, which has the effect of reducing the cation vacancy and oxide ion interstitial contents, both likely to reduce conductivities.

Slater *et al*. reported that conductivity increases with Ge content only for a single-phase hexagonal apatite, and the optimum Si/Ge ratio for high conductivity was found to be 2/4 in solid-state synthesized $La_{9.33}Si_{6-x}Ge_xO_{26}$ system.[32] In our case, Na substitution for La may play a positive role in maintaining the hexagonal structure and suppressing Ge loss, so the highest conductivity was observed for the Ge-based end-member. However, overall the conductivities are lower than observed from these prior studies, which can be related to the presence of Na reducing both cation vacancy and interstitial content. The activation energy initially increases with Ge doping and reaches the maximum at Si : Ge = 1 : 1, then drops back with further Ge doping, but the absolute change is not large. As germanate apatites usually have higher activation energies than silicates, the trend observed here for Si rich samples is accounted for by the low pellet density.

For comparison, pellets of near TD were fabricated using the SPS method. These materials showed significantly improved conductivity for Si-rich apatites, while the conductivity was similar or slightly lower than that of the conventionally sintered pellets for Ge-rich apatites, as the density discrepancies were not large (Fig. 9 (B)). In terms of the latter, the nanoscaled grain size (Fig. S3, Supporting Information) of SPS pellets may prove negative towards the total conductivity as grain boundary contributions will be more important. The biggest change in conductivity was for the Si end-member (2.17×10^{-7} to 3.66×10^{-5} $S\cdot cm^{-1}$ at 500 ºC) matching a higher pellet density (68% to 96% TD) for conventionally sintered and SPS samples. To confirm the negative effect of porosity, a less dense pellet of Si end-member apatite (83%) was made by the SPS method and the conductivity dropped by two orders of magnitude (Table 6, Fig. 9). For dense pellets composed of micron sized crystals, the bulk conductivity will be intrinsic to the material and independent of microstructure (e.g. grain

size). This may not be true for nanostructured materials and grain size will be influential. Therefore, the SPS pellets showed lower conductivity than conventionally sintered samples of similar compaction. Additionally, the conductivity decreases with Ge content, which is the opposite of conventionally sintered pellets. The corresponding activation energies for Si rich samples are relatively low (~0.88 eV) while that for Ge rich samples are much higher (~1.12 ev). As there is no significant difference in pellet density and grain size across the chemical series, and very minor Ge loss is expected as SPS does not require long sintering time, the observed conductivity changes through the series are intrinsic and controlled by both the cation vacancies and oxygen defects, with some attenuation of performance arising from the incorporation of Na^+ and possible retention of H^+.

Since the structural studies had indicated the presence of protons in the sample, some measurements were performed in different atmospheres, in particular comparing results in dry and wet N_2. The results indicated a small improvement in the conductivity in wet N_2, which for vacancy conductor systems (e.g. perovskite) can be attributed to a protonic contribution to the conductivity (Fig. S4, Supporting Information). However, as described previously,[53] the oxide ion conduction in these apatite systems is mediated by oxide ion interstitials, and the presence of water can lead to incorporation of both protons and oxide ion interstitials, and so the enhancement in this case could be due to either of these effects.

4. Conclusion

Single-phase and highly crystalline Si/Ge lanthanide oxy-hydroxyapatite powders were obtained by hydrothermal synthesis. The morphology across the series changes from nanosized spheres for Si-based end-member to hexagonal rods for Ge-based end-member.

EDS and EPMA found limited contamination by sodium, while FTIR spectroscopy and TGA proved the hydroxyl incorporation as processing artifacts. The Rietveld refinement was consistent with $P6_3/m$ structure and these electrolytes can be represented as $La_{8.50}Na_{1.29}Si_{6-x}Ge_xO_{24}(OH)_{2.79-2y}O_y\square_{y-0.79}$. Overall the conductivities were lower than conventionally synthesized systems, which can be related to the presence of Na lowering the cation vacancy and oxide ion interstitial content.

Supporting Information Available:

Powder XRD pattern (Fig. S1), *in-situ* neutron diffraction analysis (Table S1 and Fig. S2), backscattered electron micrographs of the sintered pellets (Fig. S3) and impedance spectra in dry and wet environments (Fig. S4) are provided in the Supporting Information. Also included is neutron crystallographic data in Crystallographic Information File (CIF) format for all compositions. This material is available free of charge via the Internet at http://pubs.acs.org.

Acknowledgement

The author H. Li acknowledges the Nanyang President's Graduate Scholarship (NPGS) provided by Nanyang Technological University. This work was supported by A*STAR (Agency for Science, Technology and Research) SERC Grant 082 101 0021 "Optimization of Apatite Anion Sublattices in Solid Oxide Fuel Cell Electrolytes". Spark plasma sintering (SPS) was performed at the University of New South Wales Australia with the support of Professor Sean Li.

Table 1 The atomic ratios for La, Na, and O were scaled to a total Si + Ge content of 6 atoms per formula unit, derived from quantitative EDS and EPMA for mixed Si_{6-x}/Ge_x apatites.

Nominal x	La		Na		Si		Ge		O	Departure from Nominal x (%)
	avg no.	std dev	avg no.	std dev	avg no.	std dev	avg no.	std dev	avg no.	
x=0	8.14	0.30	1.30	0.06	6.00	0.00	0.00	0.00	24.86	0.0
***x=0**	*8.47*	*0.11*	*1.24*	*0.02*	*6.00*	*0.00*	*0.00*	*0.00*	*25.33*	*0.0*
x=1	8.53	0.39	1.28	0.06	5.76	0.02	0.24	0.02	25.44	76.0
x=2	8.63	0.41	1.17	0.08	5.21	0.03	0.79	0.03	25.53	60.5
x=3	8.62	0.36	1.14	0.05	4.10	0.04	1.90	0.04	25.50	36.7
***x=3**	*8.17*	*0.09*	*1.22*	*0.02*	*4.31*	*0.06*	*1.69*	*0.06*	*24.87*	*43.7*
x=4	8.50	0.39	1.11	0.08	2.76	0.07	3.24	0.07	25.31	19.0
x=5	8.17	0.27	1.05	0.07	1.41	0.03	4.59	0.03	24.78	8.2
x=6	8.28	0.47	1.04	0.04	0.10	0.02	5.90	0.02	24.94	1.7
***x=6**	*8.31*	*0.02*	*1.42*	*0.00*	*0.06*	*0.01*	*5.94*	*0.01*	*25.18*	*1.0*

* EPMA

Table 2 Refined cell parameter data (hexagonal cell with the space group $P6_3/m$) from laboratory X-ray and neutron powder diffraction on mixed Si/Ge-based lanthanum apatites.

X-ray diffraction	Unit cell parameters (Å)		Volume (Å^3)	R (%)				GOF
Refined composition	$a = b$	c	V	R_p	R_{wp}	R_{exp}	R_b	
$La_{8.59}Na_{1.13}Si_6O_{25.45}$	9.72743(10)	7.17977(10)	588.351(14)	3.59	4.57	3.41	1.51	1.34
$La_{8.77}Na_{1.03}Si_{5.80}Ge_{0.20}O_{25.67}$	9.73420(9)	7.18823(9)	589.865(13)	3.40	4.32	3.31	1.45	1.30
$La_{8.97}Na_{0.91}Si_{5.21}Ge_{0.79}O_{25.91}$	9.74885(9)	7.19304(9)	592.038(13)	3.42	4.36	3.29	1.36	1.32
$La_{8.74}Na_{1.02}Si_{4.42}Ge_{1.58}O_{25.62}$	9.78960(15)	7.20219(13)	597.76(2)	4.12	5.39	3.28	1.62	1.64
$La_{8.70}Na_{0.98}Si_{3.22}Ge_{2.78}O_{25.54}$	9.84343(16)	7.21513(14)	605.43(2)	4.44	5.83	3.26	1.65	1.79
$La_{8.64}Na_{1.07}Si_{1.93}Ge_{4.07}O_{25.50}$	9.89589(10)	7.22902(9)	613.083(15)	3.92	5.06	3.23	1.56	1.57
$La_{8.92}Na_{0.92}Si_{0.72}Ge_{5.28}O_{25.84}$	9.93039(6)	7.23768(7)	618.106(10)	3.39	4.40	3.31	1.41	1.33
Neutron diffraction	Unit cell parameters (Å)		Volume (Å^3)	R (%)				GOF
Refined composition	$a = b$	c	V	R_p	R_{wp}	R(obs)	R(all)	
$La_{8.42}Na_{1.42}Si_6O_{25.88}H_{0.63}$	9.7272(3)	7.1816(3)	588.48(3)	2.83	3.54	4.14	4.14	1.69
$La_{8.40}Na_{1.54}Si_{5.82}Ge_{0.18}O_{26.12}H_{0.98}$	9.7332(3)	7.1863(3)	589.59(3)	3.15	3.93	4.19	4.19	1.91
$La_{8.59}Na_{1.23}Si_{5.44}Ge_{0.56}O_{25.71}H_{0.63}$	9.7503(2)	7.1955(2)	592.42(3)	3.09	3.85	4.38	4.39	1.86
$La_{8.40}Na_{1.31}Si_{4.70}Ge_{1.30}O_{25.58}H_{0.44}$	9.7912(3)	7.2058(2)	598.26(3)	2.79	3.51	3.90	3.90	1.68
$La_{8.58}Na_{1.17}Si_{2.87}Ge_{3.13}O_{25.62}H_{0.43}$	9.8442(4)	7.2185(2)	605.82(4)	3.13	3.97	4.74	4.74	1.82
$La_{8.46}Na_{1.17}Si_{1.51}Ge_{4.49}O_{26.02}H_{0.96}$	9.8973(3)	7.2309(2)	613.42(3)	3.16	3.93	3.97	3.97	1.72
$La_{8.63}Na_{1.19}Si_{0.76}Ge_{5.24}O_{25.88}H_{1.06}$	9.9451(2)	7.2431(2)	620.40(3)	3.61	4.48	4.26	4.26	1.96

Table 3 Atomic coordinates and equivalent isotropic ADPs for $La_{8.40}Na_{1.31}Si_{4.70}Ge_{1.30}O_{25.58}H_{0.44}$ from neutron powder diffraction.

Atom	Wyck	*x*	*y*	*z*	S.O.F.	U_{iso} (Å^2)
La/Na(2)	6*h*	0.2372(4)	-0.0092(4)	1/4	0.899(12)/0.101(12)	0.0216(13)
La/Na(1)	4*f*	1/3	2/3	0.4993(6)	0.753(10)/0.175(13)	0.0154(11)
Si/Ge	6*h*	0.4033(5)	0.3729(5)	1/4	0.783(14)/0.217(14)	0.0146(19)
O(1)	6*h*	0.3210(5)	0.4859(5)	1/4	1	0.034(3)
O(2)	6*h*	0.5982(5)	0.4713(5)	1/4	1	0.032(2)
O(3)	12*i*	0.3475(4)	0.2566(4)	0.0694(4)	1	0.0441(19)
O(4)	4*e*	0	0	0.1873(13)	0.396(10)	0.023(4)
H	4*e*	0	0	0.03155(6)	0.109(10)	0.02(fixed)

Space group = $P6_3/m$ (no. 176), a = 9.7912(3), c = 7.2058(2) Å. Cell volume = 598.26(3) Å^3. R_{wp} = 3.28%.

Table 4 Anisotropic ADPs for $La_{8.40}Na_{1.31}Si_{4.70}Ge_{1.30}O_{25.58}H_{0.44}$ from neutron powder diffraction.

Atom	U_{11}	U_{22}	U_{33}	U_{12}	U_{13}	U_{23} ($Å^2$)
La/Na(2)	0.0268(16)	0.0267(17)	0.0118(12)	0.0138(13)	0	0
La/Na(1)	0.0150(13)	0.0150(13)	0.0163(19)	0.0075(7)	0	0
Si/Ge	0.024(2)	0.010(2)	0.012(2)	0.0090(19)	0	0
O(1)	0.062(3)	0.046(3)	0.019(3)	0.046(3)	0	0
O(2)	0.036(3)	0.027(2)	0.030(3)	0.015(2)	0	0
O(3)	0.085(3)	0.040(2)	0.0207(13)	0.041(2)	-0.0230(13)	-0.0001(12)
O(4)	0.011(3)	0.011(3)	0.046(8)	0.0054(17)	0	0

Table 5 Selected bond lengths and angles for $La_{8.40}Na_{1.31}Si_{4.70}Ge_{1.30}O_{25.58}H_{0.44}$ from neutron powder diffraction.

Bond	Bond Length (Å)	Bond	Bond Angle (°)
La/Na(2)-O(1)	2.7684(2)	O(1)-Si/Ge-O(2)	114.470(3)
La/Na(2)-O(2)	2.4735(2)	O(1)-Si/Ge-O(3)	111.0706(16)
La/Na(2)-O(3) × 2	2.47519(13)	O(2)-Si/Ge-O(3)	107.0245(16)
La/Na(2)-O(3) × 2	2.61183(17)	O(3)-Si/Ge-O(3)	105.693(3)
La/Na(2)-O(4)	2.41098(14)		
La/Na(1)-O(1) × 3	2.48200(13)	BVS for La1	2.87
La/Na(1)-O(2) × 3	2.53867(14)	BVS for Na1	1.06
La/Na(1)-O(3) × 3	2.8700(3)	BVS for A^I* / Valence of A^I*	2.35 / 2.43
Si/Ge-O(1)	1.66261(5)	BVS for Si	3.95
Si/Ge-O(2)	1.65287(14)	BVS for Ge	5.28
Si/Ge-O(3) × 2	1.63272(8)	BVS for *B** / Valence of *B**	4.24 / 4

* BVS for A^I and *B* sites are calculated from BVS of each element, and the valences for both sites are calculated from ideal valence of each element:
BVS for $A^I = BVS_{La} \times A^I\ Occupancy_{La} + BVS_{Na} \times A^I\ Occupancy_{Na}$
BVS for $B = BVS_{Si} \times B\ Occupancy_{Si} + BVS_{Ge} \times B\ Occupancy_{Ge}$
Valence for $A^I = 3 \times A^I\ Occupancy_{La} + 1 \times A^I\ Occupancy_{Na}$
Valence for $B = 4 \times B\ Occupancy_{Si} + 4 \times B\ Occupancy_{Ge}$

Table 6 Conductivity data for pellets prepared from conventional sintering and SPS (H0–6 represent samples with nominal x = 0 – 6, and H0a & b are SPS samples of different TD).

Samples prepared by conventional sintering	Density of pellet (% theoretical)	σ (S·cm^{-1}) at 500 ºC	E_a (eV)
H0	68	2.17×10^{-7}	1.07
H1	72	2.27×10^{-7}	1.08
H2	85	1.74×10^{-7}	1.12
H3	79	1.38×10^{-7}	1.13
H4	89	3.41×10^{-7}	1.12
H5	97	1.60×10^{-6}	1.06
H6	95	8.88×10^{-6}	1.01
Samples prepared by SPS	Density of pellet (% theoretical)	σ (S·cm^{-1}) at 500 ºC	E_a (eV)
H0a	96	3.66×10^{-5}	0.87
H0b	83	1.30×10^{-7}	1.15
H1	98	1.49×10^{-5}	0.89
H2	100	1.05×10^{-5}	0.88
H3	100	3.93×10^{-6}	1.00
H4	99	1.31×10^{-6}	1.13
H5	100	8.71×10^{-7}	1.12
H6	100	7.43×10^{-7}	1.11

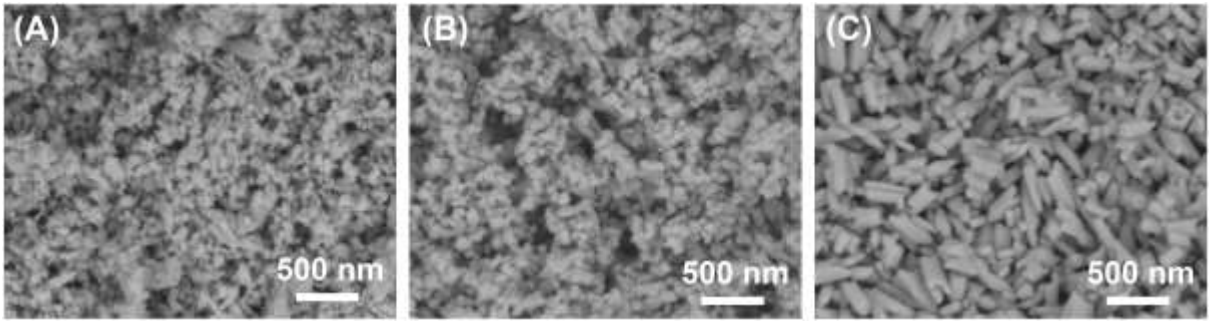

Fig. 1 Low angle backscattered electron micrographs (5.0 kV) for (A) Si end-member, (B) intermediate composition of nominal equivalent Si/Ge, and (C) Ge end-member apatites synthesized at 240 ºC for 16 hours.

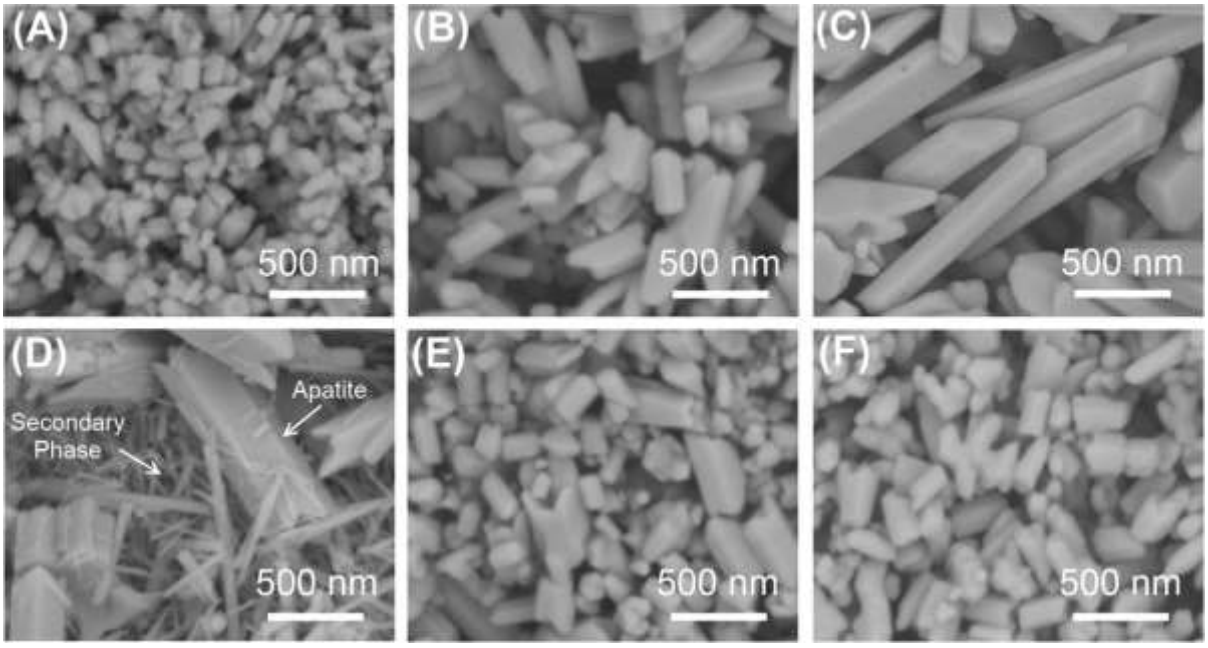

Fig. 2 Low angle backscattered electron micrographs (5.0 kV) for Ge end-member apatites with synthesis condition of (A) 220 ºC, 3 hours; (B) 220 ºC, 6 days; (C) 220 ºC, 60 days; (D) 200 ºC, 1 day; (E) 220 ºC, 1 day; (F) 240 ºC, 1 day.

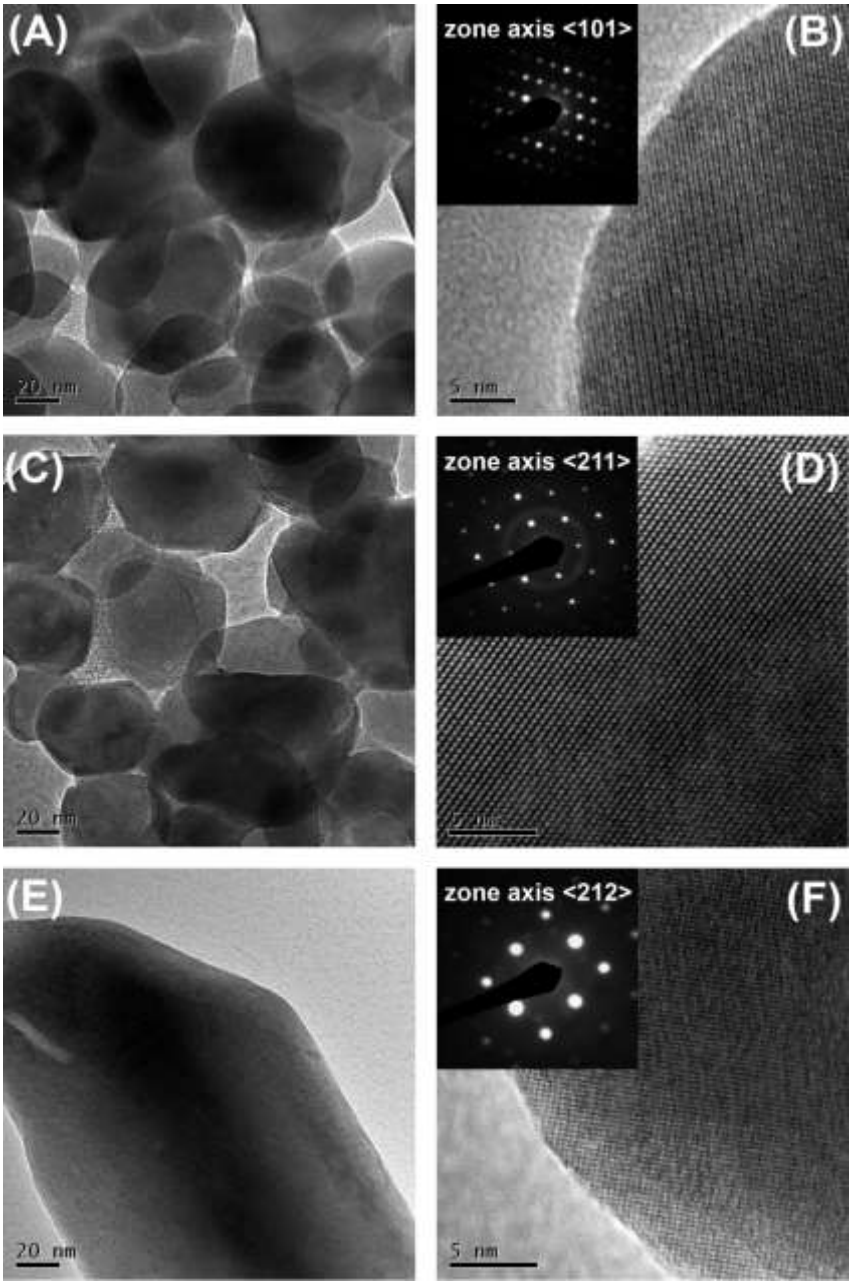

Fig. 3 TEM images (low-magnification and high-resolution) and diffraction patterns for (A) & (B) Si end-member, (C) & (D) intermediate composition of nominal equivalent Si/Ge, (E) & (F) Ge end-member apatites.

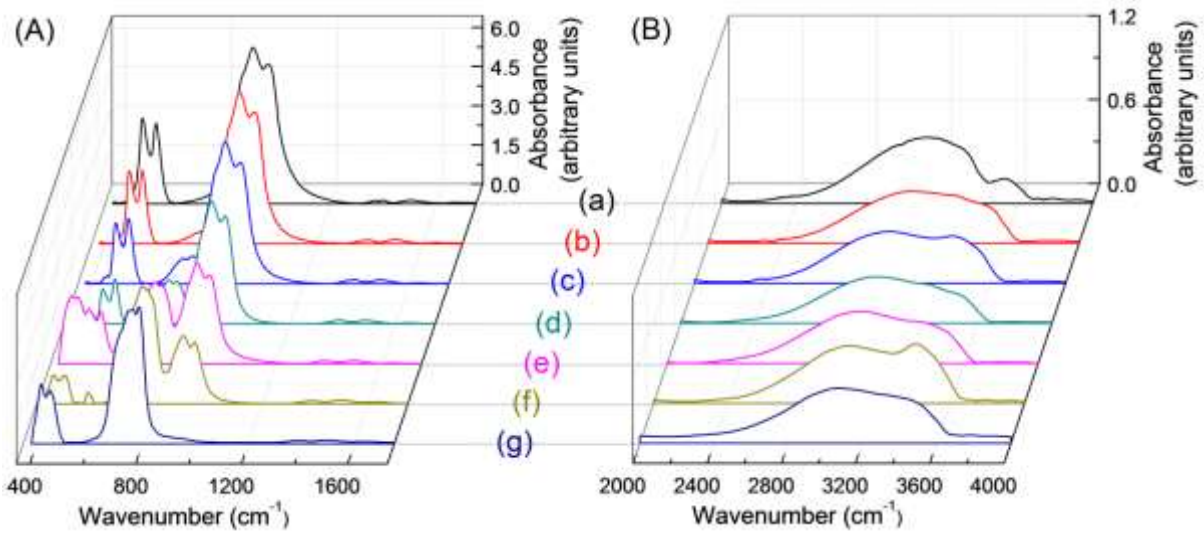

Fig. 4 FTIR spectra for mixed Si_{6-x}/Ge_x-based lanthanum apatites with wavenumber ranges from (A) 400–1800 cm^{-1} and (B) 2000–4000 cm^{-1}. The intensities were normalized to refined Si or Ge content with (a) Si_6, (b) $Si_{5.82}$, (c) $Si_{5.44}$, (d) $Si_{4.70}$, (e) $Ge_{3.13}$, (f) $Ge_{4.49}$, (g) $Ge_{5.24}$.

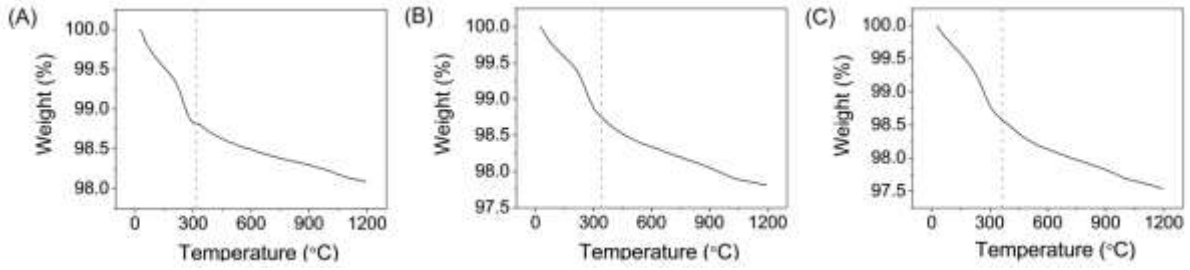

Fig. 5 TGA plots for (A) Si end-member, (B) intermediate composition of nominal equivalent Si/Ge, and (C) Ge end-member apatites synthesized at 240 ºC for 16 hours.

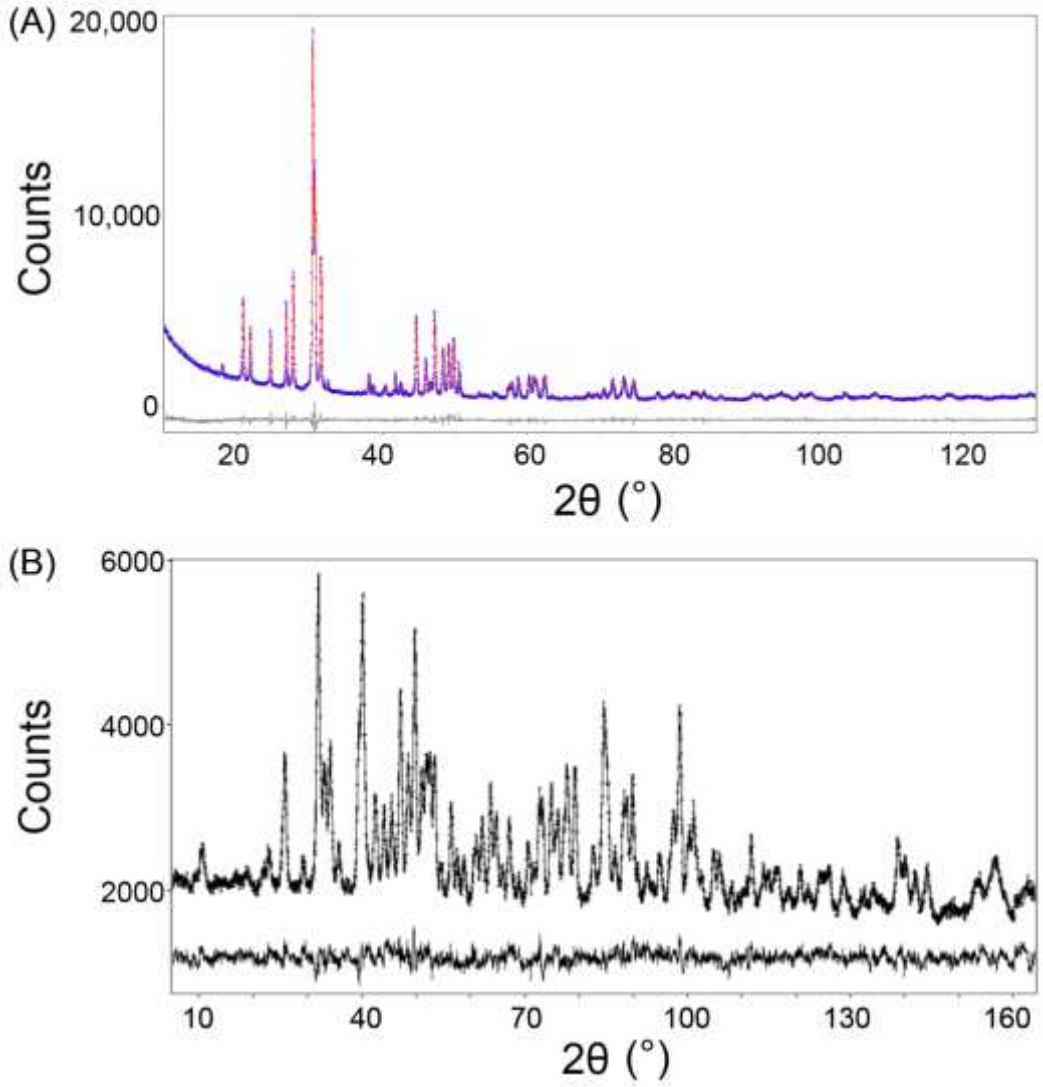

Fig. 6 Rietveld plots of the (a) laboratory X-ray and (b) neutron powder diffraction data of mixed Si_{6-x}/Ge_x–based apatite of nominal x = 3 collected at room temperature. The observed intensity is shown by dots, with the solid line representing the calculated intensity. Differences between observed and calculated intensities are plotted beneath.

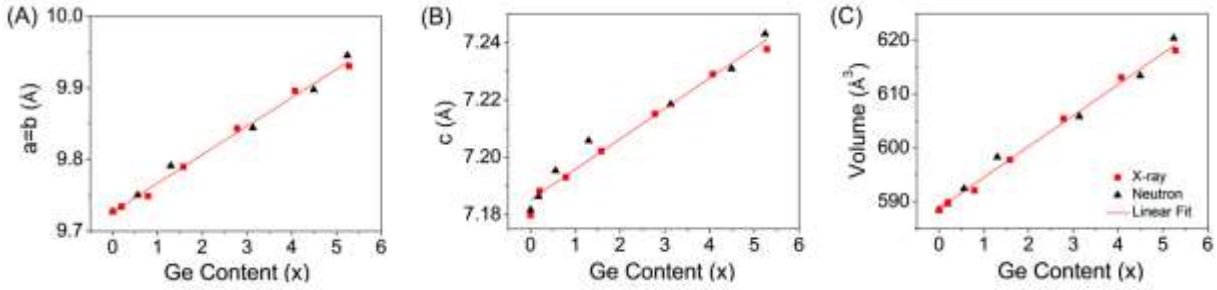

Fig. 7 Refined lattice parameters and the linear fits from powder X-ray (square) and neutron (triangle) diffraction data for the analogue of mixed Si_{6-x}/Ge_x-based lanthanum apatites with refined x from 0 – 6.

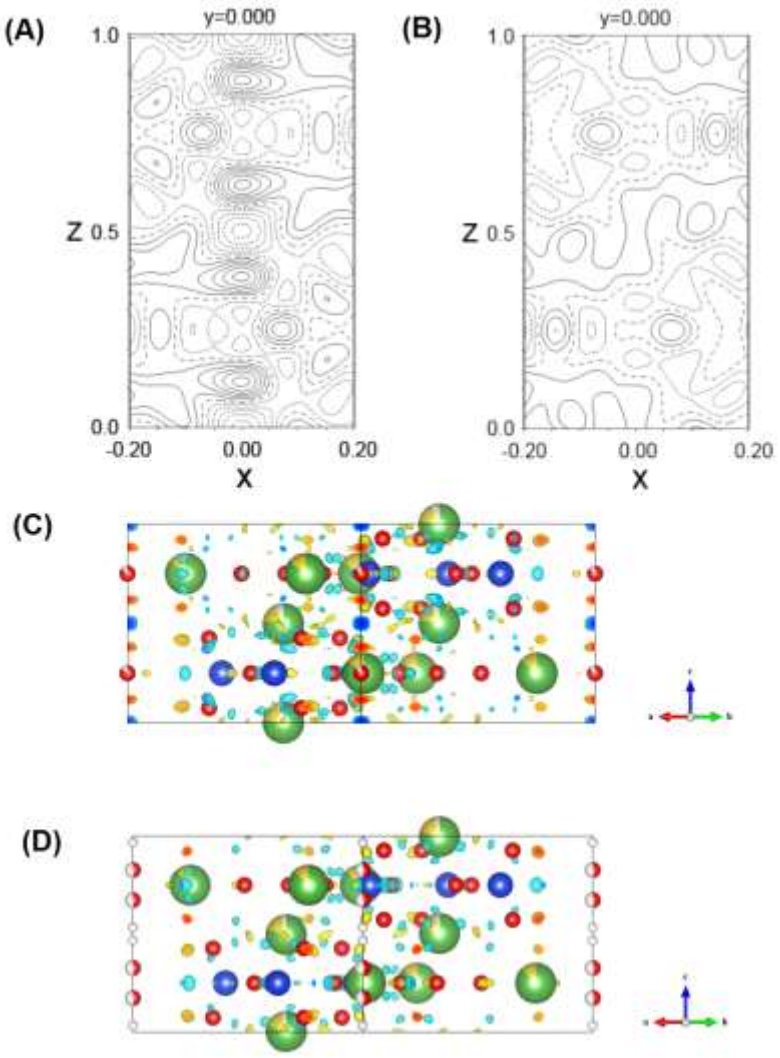

Fig. 8 2-D and 3-D Fourier mapping for the Si end-member apatite with (A) and (C) 2*a* oxygen position, (B) and (D) 4*e* oxygen and hydrogen positions.

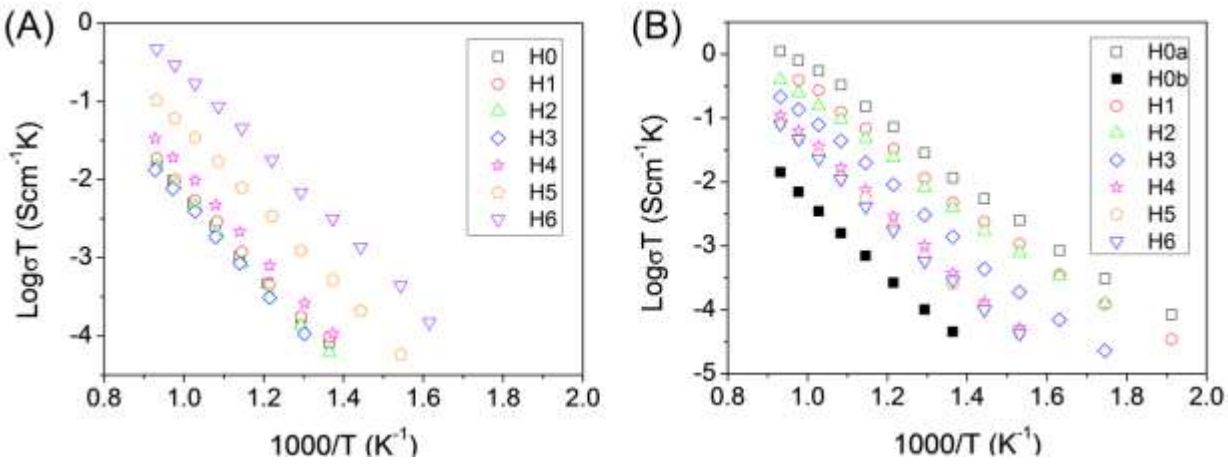

Fig. 9 Variation of conductivities with temperature for pellets of mixed Si_{6-x}/Ge_x-based lanthanum apatites (H0–6 represent samples with nominal x = 0 – 6, and H0b is the SPS sample of lower TD) prepared from (A) conventional sintering and (B) SPS.

References

(1) Nakayama, S.; Sakamoto, M. *J. Eur. Ceram. Soc.* **1998,** *18*, 1413.
(2) Nakayama, S.; Sakamoto, M. *J. Mater. Sci. lett.* **2001,** *20*, 1627.
(3) Higuchi, M.; Masubuchi, Y.; Nakayama, S.; Kikkawa, S.; Kodaira, K. *Solid State Ionics* **2004,** *174*, 73.
(4) Arikawa, H.; Nishiguchi, H.; Ishihara, T.; Takita, Y. *Solid State Ionics* **2000,** *136-137*, 31.
(5) Kharton, V. V.; Marques, F. M. B.; Atkinson, A. *Solid State Ionics* **2004,** *174*, 135.
(6) Kuo, Y.-L.; Liang, Y.-Y. *Ceram. Int.* **2012,** *38*, 3955.
(7) Slater, P. R.; Samson, J. E. H. *Diffus. Defect Data, Pt. B* **2003,** *90-91*, 195.
(8) Abram, E. J.; Sinclair, D. C.; West, A. R. *J. Mater. Chem.* **2001,** *11*, 1978.
(9) Berastegui, P.; Hull, S.; GarcI GarcI, F. J.; Grins, J. *J. Solid State Chem.* **2002,** *168*, 294.
(10) McFarlane, J.; Barth, S.; Swaffer, M.; Sansom, J. E. H.; Slater, P. R. *Ionics* **2002,** *8*, 149.
(11) Tolchard, J. R.; Sansom, J. E. H.; Islam, M. S.; Slater, P. R. *Ionics* **2004,** *10*, 353.
(12) Tolchard, J. R.; Sansom, J. E. H.; Islam, M. S.; Slater, P. R. *Dalton Trans.* **2005**, 1273.
(13) Tolchard, J. R.; Slater, P. R.; Islam, M. S. *Adv. Funct. Mater.* **2007,** *17*, 2564.
(14) Shaula, A. L.; Kharton, V. V.; Marques, F. M. B. *J. Solid State Chem.* **2005,** *178*, 2050.
(15) Li, H.; Baikie, T.; Pramana, S. S.; Shin, J. F.; Slater, P. R.; Brink, F.; Hester, J.; Wallwork, K.; White, T. J. *J. Mater. Chem.* **2012,** *22*, 2658.
(16) Beaudet-Savignat, S.; Vincent, A.; Lambert, S.; Gervais, F. *J. Mater. Chem.* **2007,** *17*, 2078.
(17) Sansom, J. E. H.; Richings, D.; Slater, P. R. *Solid State Ionics* **2001,** *139*, 205.
(18) Islam, M. S.; Tolchard, J. R.; Slater, P. R. *Chem. Commun.* **2003**, 1486.
(19) Tolchard, J. R.; Islam, M. S.; Slater, P. R. *J. Mater. Chem.* **2003,** *13*, 1956.
(20) Masubuchi, Y.; Higuchi, M.; Takeda, T.; Kikkawa, S. *Solid State Ionics* **2006,** *177*, 263.
(21) White, T. J.; Ferraris, C.; Kim, J.; Madhavi, S. *Rev. Mineral. Geochem.* **2005,** *57*, 307.
(22) Felsche, J. *J. Solid State Chem.* **1972,** *5*, 266.
(23) Sansom, J. E. H.; Kendrick, E.; Tolchard, J. R.; Islam, M. S.; Slater, P. R. *J. Solid State Electrochem.* **2006,** *10*, 562.
(24) White, T. J.; Dong, Z. *Acta Crystallogr., Sect. B: Struct. Sci.* **2003,** *59*, 1.
(25) Pramana, S. S.; Klooster, W. T.; White, T. J. *Acta Crystallogr., Sect. B: Struct. Sci.* **2007,** *63*, 597.
(26) Pramana, S. S.; Klooster, W. T.; White, T. J. *J. Solid State Chem.* **2008,** *181*, 1717.
(27) Pramana, S. S.; Baikie, T.; Kendrick, E.; Schreyer, M. K.; Slater, P. R.; White, T. J. *Solid State Ionics* **2010,** *181*, 1189.
(28) Sansom, J. E. H.; Tolchard, J. R.; Islam, M. S.; Apperley, D.; Slater, P. R. *J. Mater. Chem.* **2006,** *16*, 1410.
(29) Baikie, T.; Pramana, S. S.; Ferraris, C.; Huang, Y.; Kendrick, E.; Knight, K. S.; Ahmad, Z.; White, T. J. *Acta Crystallogr., Sect. B: Struct. Sci.* **2010,** *66*, 1.
(30) Tao, S. W.; Irvine, J. T. S. *Mater. Res. Bull.* **2001,** *36*, 1245.
(31) Sansom, J. E. H.; Hildebrandt, L.; Slater, P. R. *Ionics* **2002,** *8*, 155.
(32) Sansom, J. E. H.; Slater, P. R. *Solid State Ionics* **2004,** *167*, 23.
(33) Serra, R.; Alves, C.; Oliveira, F. A. C.; Marcelo, T.; Mascarenhas, J.; Trindade, B. *Ceram. Int.* **2012,** *38*, 5355.
(34) Kinoshita, T.; Iwata, T.; Béchade, E.; Masson, O.; Julien, I.; Champion, E.; Thomas, P.; Yoshida, H.; Ishizawa, N.; Fukuda, K. *Solid State Ionics* **2010,** *181*, 1024.
(35) Ferdov, S.; Sá Ferreira, R. A.; Lin, Z. *Chem. Mater.* **2006,** *18*, 5958.
(36) Ferdov, S.; Rauwel, P.; Lin, Z.; Ferreira, R. A. S.; Lopes, A. *J. Solid State Chem.* **2010,** *183*, 2726.

(37) Liss, K.-D.; Hunter, B.; Hagen, M.; Noakes, T.; Kennedy, S. *Physica B: Condensed Matter* **2006,** *385–386, Part 2*, 1010.
(38) Munir, Z. A.; Anselmi-Tamburini, U.; Ohyanagi, M. *J. Mater. Sci.* **2006,** *41*, 763.
(39) Hungría, T.; Galy, J.; Castro, A. *Adv. Eng. Mater.* **2009,** *11*, 615.
(40) Galy, J.; Salles, P.; Rozier, P.; Castro, A. *Solid State Ionics* **2006,** *177*, 2897.
(41) Fowler, B. O. *Inorg. Chem.* **1974,** *13*, 194.
(42) Rodríguez-Reyna, E.; Fuentes, A. F.; Maczka, M.; Hanuza, J.; Boulahya, K.; Amador, U. *J. Solid State Chem.* **2006,** *179*, 522.
(43) Kannan, R.; Mohan, S. *Mater. Sci. Eng. B* **2001,** *86*, 113.
(44) Greenwood, N. N.; Earnshaw, A. *Chemistry of the elements*. Pergamon Press: 1984.
(45) Holleman, A. F.; Wiber, E.; Wiberg, N. *Inorganic Chemistry*. Acad. Press: 2001.
(46) *X-ray Data Booklet*. Lawrence Berkeley National Laboratory, University of California: 2001.
(47) Shannon, R. D. *Acta Crystallogr., Sect. A: Cryst. Phys., Diffr., Theor. Gen. Crystallogr.* **1976,** *32*, 751.
(48) Topas V3.0; Bruker AXS GmbH: Karlsruhe, Germany, 2003.
(49) Petříček, V.; Dušek, M.; Palatinus, L. *Jana2006: The Crystallographic Computing System*, Institute of Physics, Praha, Czech Republic, 2006.
(50) An, T.; Baikie, T.; Wei, F.; Pramana, S. S.; Schreyer, M. K.; Piltz, R. O.; Shin, J. F.; Wei, J.; Slater, P. R.; White, T. J. *Chem. Mater.* **2013,** *25*, 1109.
(51) Orera, A.; Baikie, T.; Kendrick, E.; Shin, J. F.; Pramana, S.; Smith, R.; White, T. J.; Sanjuan, M. L.; Slater, P. R. *Dalton Trans.* **2011,** *40*, 3903.
(52) Panchmatia, P. M.; Orera, A.; Kendrick, E.; Hanna, J. V.; Smith, M. E.; Slater, P. R.; Islam, M. S. *J. Mater. Chem.* **2010,** *20*, 2766.
(53) Orera, A.; Slater, P. R. *Solid State Ionics* **2010,** *181*, 110.

TOC

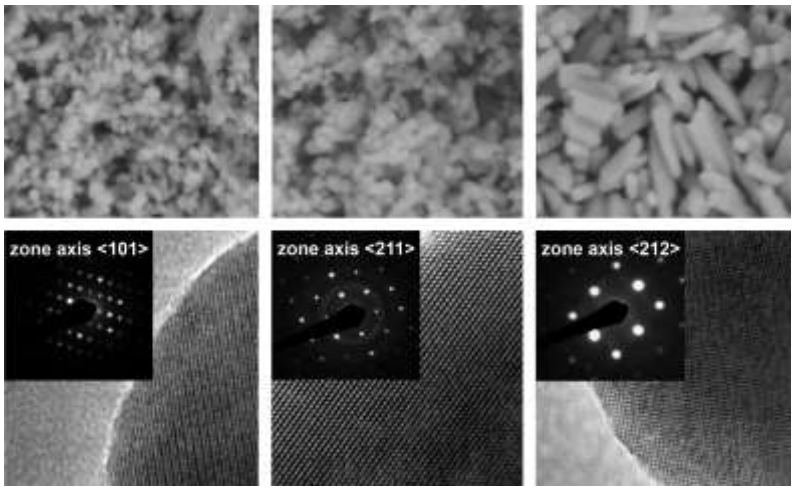

Single-phase and highly-crystalline nanosized powders of mixed Si/Ge-based apatites were obtained by hydrothermal method, the morphology changes across the series from spheres for Si-based end-member to hexagonal rods for Ge-based end-member.